PAPER

Check for updates

Rationally designed dual cocatalysts on ZnIn₂S₄ nanoflowers for photoredox coupling of benzyl alcohol oxidation with H₂ evolution†

Yu Wei,[a] Yuzheng Wu,[b] Jun Wang,[a] Yong-Hui Wu,[a] Zonglin Weng,[c] Wei-Ya Huang, [ID] [a] Kai Yang, [ID] [a] Jia-Lin Zhang, [ID] [a] Qi Li,[a] Kang-Qiang Lu [ID] *[a] and Bin Han [ID] *[c]

Constructing a dual-functional reaction platform combining photocatalytic hydrogen evolution and selective organic synthesis is an effective approach for utilizing both photogenerated electrons and holes to obtain clean, renewable fuels and high-value chemicals. Herein, we synthesized a composite photocatalyst of nickel phosphide (Ni₂P) and graphene (GR) dual cocatalyst modified zinc indium sulfide (ZnIn₂S₄) for efficient photocatalytic oxidation of benzyl alcohol (BA) coupled with hydrogen production. In this dual co-catalyst system, GR as an electron relay station can accelerate electron transfer, and Ni₂P can facilitate the separation of photogenerated carriers in the composite while providing the active site for proton reduction. As a result, the ZnIn₂S₄–GR–Ni₂P composite exhibited significantly higher activity in the photocatalytic oxidation of benzyl alcohol (BA) coupled with hydrogen production than blank ZnIn₂S₄, ZnIn₂S₄–GR, and ZnIn₂S₄–Ni₂P. This study proposes a new method of combining dual cocatalysts with semiconductor photocatalysts to simultaneously utilize photo-induced electrons and holes for synergistic coupling of photocatalytic organic synthesis and hydrogen production.

[a]Jiangxi Provincial Key Laboratory of Functional Molecular Materials Chemistry, School of Chemistry and Chemical Engineering, Jiangxi University of Science and Technology, Ganzhou, 341000, PR China. E-mail: kqlu@jxust.edu.cn

[b]School of Environmental Science and Engineering, Guangdong University of Technology, Guangzhou, 510006, PR China

[c]Guangdong Basic Research Center of Excellence for Ecological Security and Green Development, Key Laboratory for City Cluster Environmental Safety and Green Development of the Ministry of Education, School of Ecology, Environment and Resources, Guangdong University of Technology, Guangzhou, 510006, PR China. E-mail: hanbin@gdut.edu.cn

† Electronic supplementary information (ESI) available. See DOI: https://doi.org/10.1039/d4ta02289k

Bin Han received his PhD in environmental science and chemical engineering from the South China University of Technology. He currently works as a professor at the School of Ecology, Environment and Resources, Guangdong University of Technology. His main research interests include environmental functional materials, chemicals and technologies for water treatment and artificial photosynthesis.

Bin Han

1 Introduction

Hydrogen fuel with its pollution-free and high-quality energy density is an important clean energy source.[1–6] Converting solar energy into hydrogen energy through semiconductor photocatalysts is one of the best methods for dealing with energy and environmental challenges.[7–10] In traditional photocatalytic hydrogen production processes, photo-generated electrons can reduce protons to generate hydrogen, while photo-generated holes are generally consumed by sacrificial agents.[11,12] Although the addition of sacrificial agents in the reaction system can effectively enhance the hydrogen production rate, the oxidizing ability of holes is not effectively utilized. Meanwhile, the use of expensive sacrificial agents greatly hinders the economic benefits and application prospects of photocatalytic hydrogen production half-reactions. By exploiting photoredox coupling of benzyl alcohol oxidation with the H₂ evolution reaction, the light-excited electron–hole pairs can be exploited simultaneously, which avoids the use of additional sacrificial agents and wastes the energy of holes.[13–15] Although there are some reports on such dual-functional catalyst reactions in recent years, issues such as doping with precious metals or low carrier separation efficiency still exist. Therefore, developing inexpensive and highly active catalytic materials remains an important and highly challenging task.

Zinc indium sulfide (ZnIn₂S₄) as a bimetallic sulfide photocatalyst has shown favorable prospects due to its good visible

18986 | *J. Mater. Chem. A*, 2024, **12**, 18986–18992

This journal is © The Royal Society of Chemistry 2024

light absorption capability and chemical stability.[16–21] However, its fast photo-induced carrier recombination and absence of active sites have limited its further application.[22–25] To address this issue, introducing appropriate co-catalysts is a practical method.[26–28] Due to the favorable electrical conductivity properties and chemical stabilities, graphene (GR) can be used as a co-catalyst to accelerate the transfer of the photo-induced carriers of the semiconductor.[29–31] Moreover, the nickel phosphide (Ni_2P) cocatalyst has been widely investigated in recent years due to its metal-like properties with benign conductivity.[32–34] Ni_2P has a strong binding capacity for protons or hydrides, but the adsorption for hydrogen is weak, which means it can be used as a superior active site for H_2 production.[35,36] Therefore, rationally compositing GR and Ni_2P dual cocatalysts with $ZnIn_2S_4$ will be an effective means to boost the photocatalytic performance of $ZnIn_2S_4$ toward photoredox coupling of benzyl alcohol oxidation with H_2 evolution.

Herein, GR and Ni_2P dual cocatalyst modified $ZnIn_2S_4$ nanoflowers have been prepared by simple hydrothermal and *in situ* photo deposition processes. The developed ternary composites can simultaneously utilize photogenerated electrons and holes to actuate the oxidation of benzyl alcohol (BA) to benzaldehyde (BAD) integrated with H_2 evolution. With a hydrogen production rate of 1287.8 $\mu mol\ g^{-1}\ h^{-1}$ and a benzyl alcohol conversion rate of 100%, the $ZnIn_2S_4$–GR–Ni_2P composite outperforms most analogous hybrid cocatalyst systems in the literature and $ZnIn_2S_4$, $ZnIn_2S_4$–GR, and $ZnIn_2S_4$–Ni_2P. The synergy of the dual cocatalysts in enhancing the transfer of charge carriers and accelerating the surface reaction is the fundamental cause of the superior visible-light photoactivity and selectivity over the $ZnIn_2S_4$–GR–Ni_2P composite. We hope that this work can facilitate the rational design of semiconductor-based photocatalysts for the sustainable production of visible-driven clean hydrogen energy and value-added chemicals.

2 Experimental

2.1 Materials

Sodium hypophosphite (NaH_2PO_2), indium chloride ($InCl_3$), benzaldehyde (C_7H_6O, BAD), benzyl alcohol (C_7H_8O, BA), thioacetamide (TAA, 99%), 5,5-dimethyl-1-pyrroline-*N*-oxide (DMPO), and carbon tetrachloride (CCl_4) were bought from Macklin Biochemical Co., Ltd (Shanghai, China). Ethanol (C_2H_5OH), zinc nitrate hexahydrate ($Zn(NO_3)_2 \cdot 6H_2O$), and triethanolamine ($C_6H_{15}NO_3$, TEOA) were supplied by Xilong Scientific Co., Ltd. Cetyltrimethyl ammonium bromide (CTAB) was bought from Shanghai Qingxi Chemical Technology Co., Ltd. Nickel(II) nitrate hexahydrate ($Ni(NO_3)_2 \cdot 6H_2O$) and acetonitrile (MeCN) were provided by Sinopharm Chemical Reagent Co., Ltd (Shanghai, China).

2.2 Synthesis of $ZnIn_2S_4$–GR–Ni_2P (ZIS–GR–Ni_2P)

The synthetic process of $ZnIn_2S_4$ (ZIS), graphene oxide (GO), and $ZnIn_2S_4$–GR (ZIS–GR) is presented in the ESI.† Using an *in situ* photochemical deposition technique, ZIS–GR–Ni_2P was

obtained. Typically, sufficient sonication was used to first disperse 60 mg of the produced ZIS–GR in 20 mL of DI, and then a calculated amount of $Ni(NO_3)_2 \cdot 6H_2O$ and NaH_2PO_2 was added. Following a 40 minute nitrogen (N_2) bubbling process to remove any air from the mixture, the yellow suspension was stirred and exposed to visible light ($\lambda \geq 420$ nm) for 20 minutes. After illumination, the precipitate was retrieved *via* filtering and rinsed three times with deionized water. Finally, the sample was fully dried at 333 K in a vacuum.

2.3 Synthesis of $ZnIn_2S_4$–Ni_2P (ZIS–Ni_2P)

Except for substituting ZIS for ZIS–GR, the preparation process for ZIS–Ni_2P was the same as that for ZIS–GR–Ni_2P.

2.4 Photocatalytic activity tests

Typically, a quartz reactor was filled with photocatalysts (5 mg), 0.1 mmol BA, and 10 mL DI water. The mixture was sonicated for two minutes before irradiation, and then purged for 30 minutes using N_2 gas to get rid of air. Subsequently, the mixture indicated above was exposed to visible light ($\lambda \geq 420$ nm) using a 300 W Xe arc lamp (Microsolar300, Beijing Perfectlight). Similar to the above photoredox-catalyzed BA conversion integrated with H_2 evolution, photoactivity of quenching experiments was investigated with the addition of various scavengers (DMPO as the scavenger for free radical species, TEOA as the scavenger for photogenerated holes, and CCl_4 as the scavenger for photogenerated electrons). The only difference was that scavengers (0.1 mmol) were added to the reaction system. An electrical fan maintained the reactor's temperature at room temperature. After 2 h, the gaseous products were subjected to gas chromatography analysis (GC 7900, Techcomp). A thermal conductivity detector (TCD) was used to measure H_2. Simultaneously, following the reaction, a 0.22 μm filter membrane was used to filter the solid catalyst, and the concentration trend of benzyl alcohol and benzaldehyde was analyzed by high-performance liquid chromatography. For cycling stability experiments, following the initial reaction under visible light irradiation, the photocatalyst was separated by filtration and then rinsed three times with deionized water. The used catalyst is then mixed with a new reaction solution for the second test of photocatalytic activity. Repeat the above steps five times to explore the stability of the sample.

3 Results and discussion

The synthetic diagram of the ZIS–GR–Ni_2P ternary composite is presented in Fig. 1a. Initially, the ZIS–GR composite has been synthesized by *in situ* growth of ZIS on GR by the one-step hydrothermal method, followed by the *in situ* photo-deposition of Ni_2P onto the surface of ZIS–GR to obtain the ZIS–GR–Ni_2P ternary composite. The *in situ* growth ensures a tight interfacial contact between ZIS and GR. Field emission scanning electron microscopy (FESEM) has been used to study the morphology of various materials. The SEM image of blank ZIS shown in Fig. 1b reveals that the pure ZIS has a nanoflower structure with a radius of about 500 nm.[37–39] As shown in
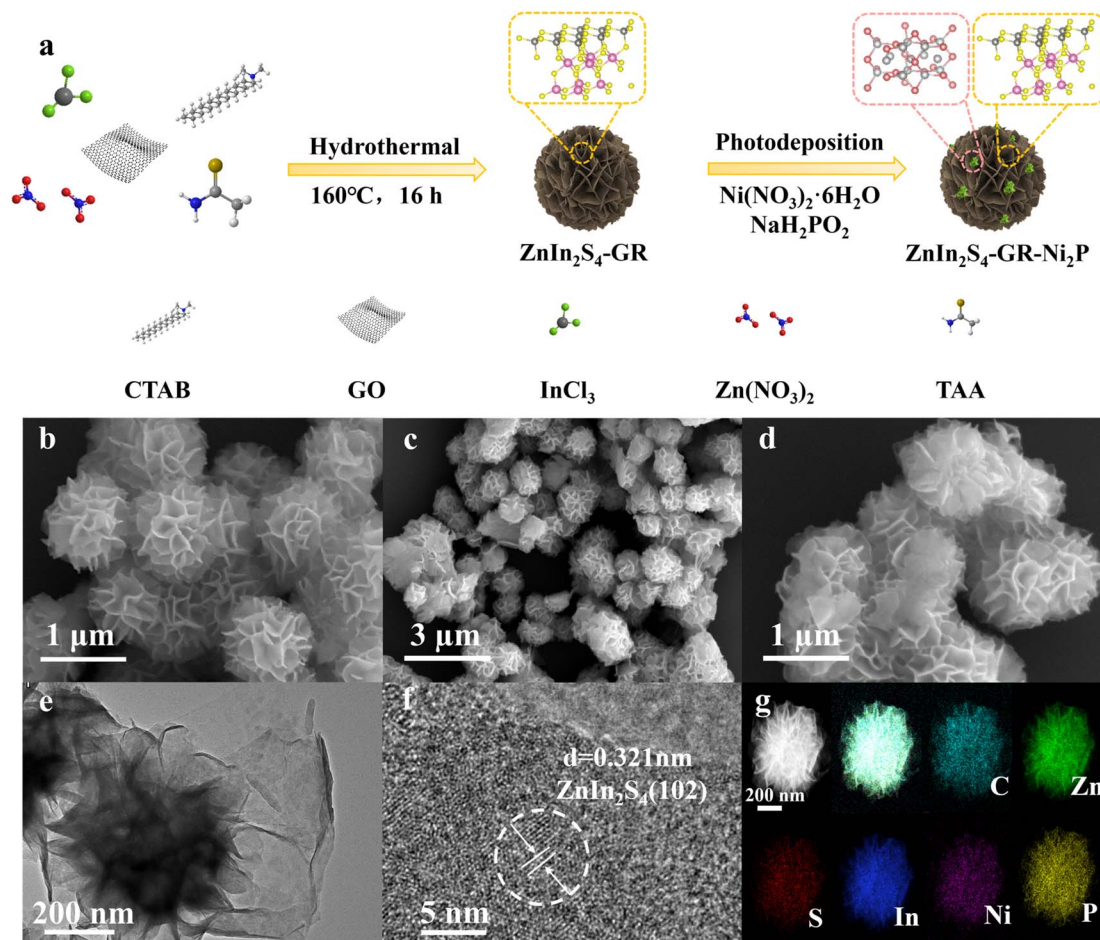
This journal is © The Royal Society of Chemistry 2024

J. Mater. Chem. A, 2024, **12**, 18986–18992 | **18987**

Fig. 1 Diagrammatic depiction of the synthesis of ZIS−GR−Ni$_2$P (a). FESEM images of ZIS (b) and ZIS−GR−Ni$_2$P (c and d). and TEM image of ZIS−GR−Ni$_2$P. (e and f) Elemental mapping results of ZIS−GR−Ni$_2$P and the HRTEM image (g).

Fig. S1a and b,† pure ZIS is uniformly covered by GR. These images indicate the successful composite of GR and ZIS photocatalysts. The SEM images of ZIS–Ni$_2$P (Fig. S2a and b†) and the ternary ZIS–GR–Ni$_2$P composite (Fig. 1c and d) indicate Ni$_2$P is highly dispersed and large Ni$_2$P particles have not been observed. The ZIS–GR–Ni$_2$P composite's successful synthesis has been further confirmed using high-resolution transmission electron microscopy (HRTEM). According to Fig. 1e and f, the lattice fringe of 0.321 nm is attributed to the (102) crystal facet of ZIS and the Ni$_2$P synthesized by the light-deposition method is amorphous.[40] Furthermore, the element mapping results in Fig. 1g indicate that C, Zn, S, In, Ni, and P elements are consistently distributed in the ZIS–GR–Ni$_2$P composite, suggesting that Ni$_2$P is uniformly deposited onto the surface of ZIS–GR microspheres.

Crystal structure information of the samples has been collected through the use of X-ray powder diffraction (XRD). Fig. 2a exhibits the XRD spectra of ZIS, ZIS–GR, ZIS–Ni$_2$P, and ZIS–GR–Ni$_2$P. Fig. 2a shows that the primary ZIS diffraction peaks occur at 2θ values of 21.5°, 28.3°, and 47.2°, respectively. These values correspond to the crystal facets of hexagonal ZIS (JCPDS No. 65-2023) at (006), (102), and (110).[40] No

characteristic diffraction peaks of GR are detected in the XRD spectra of binary ZIS–GR and ternary ZIS–GR–Ni$_2$P samples, which is a result of the weak peak and low content intensity of GR. Furthermore, the characteristic diffraction peak of Ni$_2$P has also not been observed, which is because of the amorphous nature of the photo-deposited Ni$_2$P.[34,41] The properties regarding optical absorption of the samples have been examined using the UV-visible diffuse reflectance spectra (DRS). ZIS displays noticeable absorption edges at a wavelength of about 510 nm, which corresponds to the inherent band gap absorption, as seen in Fig. 2b. Additionally, ZIS's band gap value is determined to be 2.63 eV using the Kubelka–Munk function (Fig. S3†).[42] After loading of GR and Ni$_2$P, the visible light region absorbance of ZIS gradually increased.

The samples' element composition and valence state have been examined by utilizing X-ray photoelectron spectroscopy (XPS). The energy spectrum diagram of the ZIS–GR–Ni$_2$P composite in Fig. S4a† reveals the presence of S, Zn, In, Ni, P, and C elements, consistent with the results of TEM elemental mapping. As shown in Fig. S4b,† by comparison with the XPS spectrum diagram of GO (Fig. S4c†), it can be inferred that the peak intensity of oxygen functional groups in ZIS–GR–Ni$_2$P is
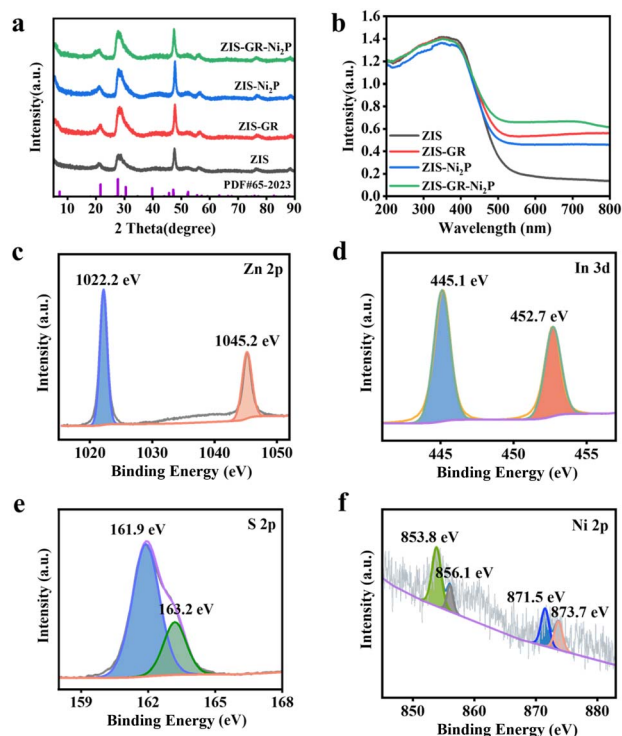
Fig. 2 XRD patterns (a) and DRS spectra (b) of ZIS, ZIS–GR, and ZIS–Ni$_2$P. XPS spectra of Zn 2p (c), In 3d (d), S 2p (e), and Ni 2p (f) of the ZIS–GR–Ni$_2$P composite.
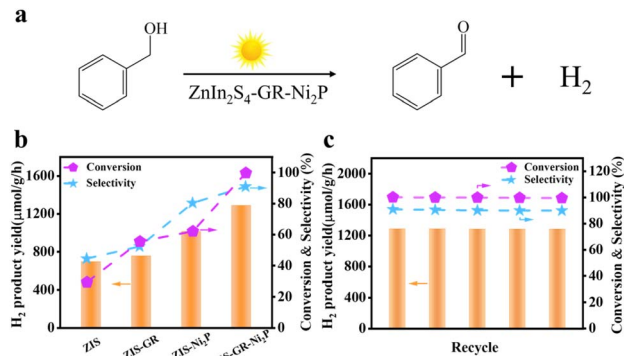

Fig. 3 The photocatalytic activity formula for selective BA oxidation in conjunction with H$_2$ evolution tests (a). Photocatalytic activity data of blank ZIS, ZIS–GR, ZIS–Ni$_2$P, and ZIS–GR–Ni$_2$P for selective BA oxidation along with the H$_2$ evolution reaction (b). Result of the cycle tests over ZIS–GR–Ni$_2$P (c).

lower, indicating the effective reduction of GO during the process of hydrothermal synthesis.[29,43,44] As depicted in Fig. 2c, the peaks of Zn in ZIS at 1045.2 eV and 1022.2 eV correspond to Zn 2p$_{1/2}$ and Zn 2p$_{3/2}$, respectively, implying the presence of Zn^{2+}. The presence of In^{3+} in the sample is indicated by the peaks in Fig. 2d at 452.7 eV and 445.1 eV, which correspond to In 3d$_{3/2}$ and In 3d$_{5/2}$, respectively. In Fig. 2e, the peaks at 162.7 eV and 161.4 eV belong to S 2p$_{1/2}$ and S 2p$_{3/2}$, confirming the presence of S^{2-}. Furthermore, as shown in Fig. 2f, the two main peaks at 871.5 eV and 853.8 eV belong to Ni 2p$_{1/2}$ and Ni 2p$_{3/2}$, respectively, accompanied by the satellite peaks at 873.7 eV and 856.1 eV, indicating the presence of Ni^{2+}.[43] As demonstrated in Fig. S4d,† the peak at 134.4 eV belongs to the P of Ni$_2$P, while the peak at 128.9 eV belongs to phosphorus oxide formed by surface oxidation during the testing process.[42]

The photocatalytic performance of blank ZIS, ZIS–GR, ZIS–Ni$_2$P, and the ZIS–GR–Ni$_2$P composite has been evaluated through photoredox coupling of benzyl alcohol oxidation with the H$_2$ evolution reaction (Fig. 3a). As shown in Fig. 3b, the hydrogen evolution efficiency (694.9 μmol g^{-1} h^{-1}), benzyl alcohol conversion rate (29.6%), and benzaldehyde selectivity (44.5%) of blank ZIS are relatively low.[45,46] After the introduction of GR or Ni$_2$P, the photocatalytic activity of ZIS–GR or ZIS–Ni$_2$P can be improved. When co-catalysts GR and Ni$_2$P have been simultaneously introduced, the ZIS–GR–Ni$_2$P ternary composite exhibits the most superior photocatalytic activity, with a hydrogen evolution efficiency of 1287.8 μmol g^{-1} h^{-1}, 100% benzyl alcohol conversion, and 90.9% benzaldehyde selectivity.

Furthermore, in comparison with previous research, the ZIS–GR–Ni$_2$P system exhibits superior behavior of photochemical selective conversion of BA to BAD and simultaneous hydrogen production (Table S1†).

To assess the stability of the ZIS–GR–Ni$_2$P composite, a cycling test has been conducted. As depicted in Fig. 3c, the ZIS–GR–Ni$_2$P composite exhibits good stability after five cycles with no discernible deactivation. Moreover, as shown in Fig. S5a,† the SEM image of the used ZIS–GR–Ni$_2$P composite reveals that the morphological structure of the nanoflower sphere remains unchanged. Furthermore, the XRD pattern of the used ZIS–GR–Ni$_2$P composite, as depicted in Fig. S5b,† is identical to the crystal structure before the reaction, providing further evidence of the excellent crystalline phase stability of the ZIS–GR–Ni$_2$P composite. Furthermore, as shown in Table S2,† the ICP-OES test of the reaction solution over the ZIS–GR–Ni$_2$P composite indicates that there is no obvious leaching of metal ions (Zn^{2+} and Ni^{2+}) during the recycling test. These results indicate that the ZIS–GR–Ni$_2$P composite is a stable catalyst for photoredox coupling of benzyl alcohol oxidation with H$_2$ evolution.[14]

N$_2$ adsorption–desorption isotherms have been used to calculate the sample's specific surface area and pore size distribution curve.[11] As shown in Fig. 4a, the curves of blank ZIS, ZIS–GR, ZIS–Ni$_2$P, and ZIS–GR–Ni$_2$P are a typical type IV isotherm and the significant increase in adsorption capacity in the high-pressure region indicates that these samples all have mesoporous structures. According to the pore size distribution plot in Fig. S6,† the mesoporous distribution probability of ZIS–GR–Ni$_2$P is considerably greater than that of ZIS, ZIS–GR, and the ZIS–Ni$_2$P composite. Furthermore, as indicated in Table S3,† the specific surface area and pore volume of the ZIS–GR–Ni$_2$P composite are the largest, indicating that introducing a dual cocatalyst can increase the specific surface area and expose more reactive sites of ZIS. As illustrated in Fig. S7,† the contact angle test is used to measure the hydrophilicity of prepared materials. Generally, the smaller the contact angle, the better the hydrophilicity of the cocatalyst. The contact angle of
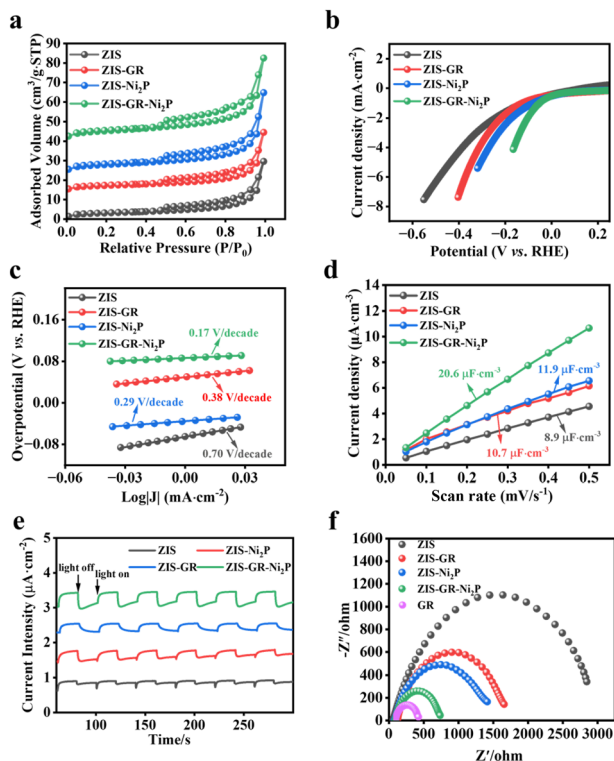
Fig. 4 Nitrogen adsorption–desorption isotherms (a), polarization curves (b), Tafel slope diagram (c), plots of capacitance current *versus* scan rate measured (d), transient photocurrent spectra (e) and EIS Nyquist plots (f) of blank ZIS, ZIS–GR, ZIS–Ni$_2$P, and ZIS–GR–Ni$_2$P.

ZIS–GR–Ni$_2$P is the smallest, indicating that the ternary composite can absorb more water molecules and rapidly release hydrogen bubbles, reducing the blocking area and exposing more surface active sites, which contributes to reinforced photocatalytic hydrogen production activity.

The photoelectrochemical tests have been used to reveal the correlation between the enhancement of the photocatalytic performance and the separation and transfer efficiency of photogenerated carriers of the obtained samples.[47] As depicted in Fig. 4b, the polarization curves (LSV) of blank ZIS, ZIS–GR, ZIS–Ni$_2$P, and ZIS–GR–Ni$_2$P are presented, and it can be observed that the ternary composite requires the lowest overpotential when reaching the same current density. In addition, the Tafel slope is obtained after linear fitting. Fig. 4c shows that the slope of ZIS–GR–Ni$_2$P is much lower than that of ZIS, ZIS–GR, and ZIS–Ni$_2$P, indicating faster reaction kinetics and better interface charge efficiency over ZIS–GR–Ni$_2$P. In addition, Fig. S8† illustrates the cyclic voltammetry (CV) curves of ZIS, ZIS–GR, ZIS–Ni$_2$P, and ZIS–GR–Ni$_2$P, respectively. As seen in Fig. 4d, the double-layer capacitance (20.6 μF cm^{-2}) of the ZIS–GR–Ni$_2$P composite is significantly larger than that of blank ZIS (8.9 μF cm^{-2}), ZIS–GR (10.7 μF cm^{-2}), and ZIS–Ni$_2$P (11.9 μF cm^{-2}), indicating that introducing GR and Ni$_2$P increases the reaction surface area and exposes more reaction sites of the ternary ZIS–GR–Ni$_2$P composite. As demonstrated in Fig. 4e, the transient photocurrent–time curve of ZIS, ZIS–GR, ZIS–Ni$_2$P, and the ZIS–GR–Ni$_2$P composite reveals that the sample ZIS–

GR–Ni$_2$P has significantly higher photocurrent response intensity than the other samples, indicating that its charge transfer rate is the fastest and the separation efficiency of photogenerated carriers is the highest.[48] Studies using electrochemical impedance spectroscopy (EIS) have been carried out to gain a thorough understanding of the charge migration at the catalyst–electrolyte interface (Fig. 4f).[49] Among the three catalysts, ZIS–GR–Ni$_2$P has the smallest curvature radius, indicating that the resistance of ZIS–GR–Ni$_2$P in the process of charge transfer is the smallest. To further investigate the separation ability of photogenerated electron–hole pairs, a steady-state photoluminescence (PL) spectrum test has been conducted on the samples. As shown in Fig. 5a, the PL intensity of ZIS–GR–Ni$_2$P is the lowest, indicating that introducing a dual cocatalyst can enhance the separation efficiency of photogenerated carriers and suppress carrier recombination, thereby enhancing the photocatalytic activity of the sample.

Control experiments have been carried out to reveal the mechanism of benzyl alcohol oxidation coupled with the hydrogen evolution reaction. As shown in Fig. 5b and c, the photocatalytic reaction is proven to be light-driven by the fact that the reaction cannot continue after removing the photocatalyst or visible light irradiation. Adding CCl$_4$ as an electron scavenger hinders the production of H$_2$, while adding the hole scavenger triethanolamine (TEOA) stops the generation of benzaldehyde, indicating that photogenerated electrons and holes are involved in the generation of H$_2$ and benzaldehyde, respectively. Furthermore, the generation of benzaldehyde is strongly inhibited by 5,5-dimethyl-1-pyrroline-*N*-oxide (DMPO), indicating that a free radical intermediate is involved in the formation of benzaldehyde.[50,51] In addition, the effect of different BA solution concentrations on the reaction has been investigated. As depicted in Fig. S9,† the activity of the ZIS–GR–Ni$_2$P composite remains unvaried after the concentration of BA
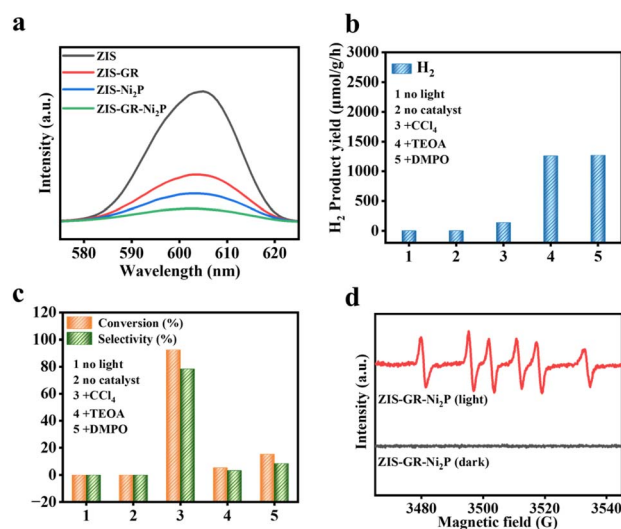

Fig. 5 Steady-state photoluminescence (PL) emission spectra of the obtained samples (a). Results of controlled experiments with different trapping agents over ZIS–GR–Ni$_2$P (b and c). EPR spectra over the ZIS–GR–Ni$_2$P composite (d).

18990 | *J. Mater. Chem. A*, 2024, **12**, 18986–18992

This journal is © The Royal Society of Chemistry 2024

is changed. To gain more understanding of the photocatalytic mechanism of this cooperative reaction system, the active intermediate over the ZIS–GR–Ni$_2$P composite is identified using the electron paramagnetic resonance (EPR) technique with DMPO acting as the radical scavenger. As disclosed in Fig. 5d, the absence of signal peaks in the dark reaction state suggests that light is necessary for the production of free radicals. After the reaction system is exposed to visible light radiation, the sextet peaks that are associated with the DMPO-trapped carbon-center radical (α-hydroxybenzyl, Cα) are observed, proving that α-hydroxybenzyl is the main intermediate in this system.[11,45]

As shown in Fig. S10a,† ZIS displays an n-type semiconductor trend when viewed in the context of the Mott–Schottky curves, with its flat band potential fixed at −0.63 V *vs.* Ag/AgCl. Since the conduction band (CB) position of an n-type semiconductor is closer to its flat band potential, the CB position of ZIS is therefore projected to be −0.43 V *vs.* NHE. With respect to the band gap data that were previously acquired, the valence band (VB) position of ZIS is determined to be 2.2 V *vs.* NHE, using the formula $E_{VB} = E_{CB} + E_g$ (where E_{VB}, E_{CB}, and E_g represent the energy values of the VB, CB, and band gap separately).[52] In addition, as shown in Fig. S10b,† the Fermi energy level of GR is −0.28 V (*vs.* NHE, pH = 7). In light of the aforementioned findings, we propose a possible mechanism for BA conversion combined with H$_2$ evolution over ZIS–GR–Ni$_2$P. As shown in Fig. 6, ZIS in the ZIS–GR–Ni$_2$P composite is initially excited to produce electrons and holes upon exposure to visible light, and the electrons then migrate from ZIS's conduction band (CB) to GR. Afterwards, Ni$_2$P anchored on ZIS–GR can further capture and transfer photo-generated electrons located on GR. H$_2$ is created when these photogenerated electrons on Ni$_2$P combine with protons in water. Meanwhile, the photogenerated holes located in ZIS first oxidize BA, leading to BA dehydrogenation to form a carbon-centered radical (·CH(OH)Ph), which is then oxidized to produce BAD. Due to the introduction of the dual cocatalyst, the photoexcited electron–hole pair can be effectively separated, which leads to a more efficient and timely oxidation of the carbon-centered radical into BAD and reduces the formation of C–C coupling byproducts, thus presenting the high selectivity of BAD over the ZIS–GR–Ni$_2$P composite.[51,53]
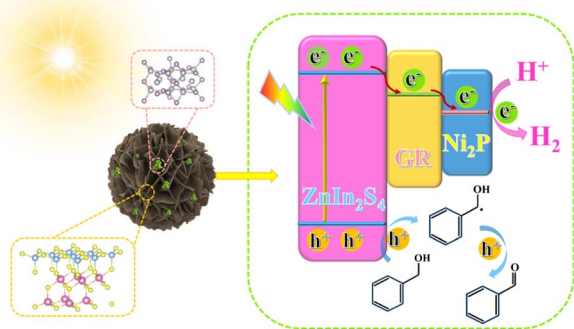

Fig. 6 Mechanism diagram of BA selective oxidation along with H$_2$ generation over ZIS–GR–Ni$_2$P.

4   Conclusions

In summary, we have synthesized a low-cost and highly efficient ternary ZIS–GR–Ni$_2$P composite by using hydrothermal and photo-deposition methods for the selective conversion of BA to BAD and simultaneous H$_2$ production. The ternary composite exhibits the best photocatalytic activity, with a hydrogen production rate of 1287.8 μmol g^{-1} h^{-1} and a benzyl alcohol conversion rate of 100%, which is 3.3 times that of the blank ZIS, and a benzaldehyde selectivity of 90.9%. Mechanism research shows that Ni$_2$P not only provides active sites for H$_2$ generation but also enhances the transfer of photogenerated electrons from ZIS, while GR also plays a critical role in accelerating the electron transfer process. This work may provide new insights into the decoration of semiconductor photocatalysts with earth-abundant dual-cocatalysts for simultaneously using photoexcited electrons and holes to acquire valuable fine chemicals and H$_2$ fuel.

Author contributions

Yu Wei: investigation, methodology, data curation, formal analysis, visualization, writing – original draft. Yuzheng Wu: investigation. Jun Wang: methodology, investigation. Yong-Hui Wu: investigation. Wei-Ya Huang: conceptualization. Zonglin Weng: methodology, investigation. Kai Yang: investigation. Jia-Lin Zhang: formal analysis. Kang-Qiang Lu: conceptualization, funding acquisition, project administration, supervision, writing – review & editing. Bin Han: conceptualization, project administration, supervision, writing – review & editing.

Conflicts of interest

There are no conflicts to declare.

Acknowledgements

Notes and references

1   Y. Luo, B. Zhang, C. Liu, D. Xia, X. Ou, Y. Cai, Y. Zhou, J. Jiang and B. Han, *Angew. Chem., Int. Ed.*, 2023, **62**, e202305355.

2   X. Feng, H. Shang, J. Zhou, X. Ma, X. Gao, D. Wang, B. Zhang and Y. Zhao, *Chem. Eng. J.*, 2023, **457**, 141192.

3   Y. Li, L. Wang, X. Gao, Y. Xue, B. Li and X. Zhu, *J. Mater. Chem. A*, 2024, **12**, 7807–7816.

4   X. Hao, W. Deng, Y. Fan and Z. Jin, *J. Mater. Chem. A*, 2024, **12**, 8543–8560.

This journal is © The Royal Society of Chemistry 2024

J. Mater. Chem. A, 2024, **12**, 18986–18992 | **18991**

5 J. Jiang, Z. Xiong, H. Wang, G. Liao, S. Bai, J. Zou, P. Wu, P. Zhang and X. Li, *J. Mater. Sci. Technol.*, 2022, **118**, 15–24.

6 J. Chen, Y. Tang, S. Wang, L. Xie, C. Chang, X. Cheng, M. Liu, L. Wang and L. Wang, *Chin. Chem. Lett.*, 2022, **33**, 1468–1474.

7 X.-X. Li, X.-C. Liu, C. Liu, J.-M. Zeng and X.-P. Qi, *Tungsten*, 2023, **5**, 100–108.

8 B. Zhao, B. Zhang, X. Liu, Z. Mou, B. Wang, Z. Wang and Q. Wang, *J. Mater. Chem. A*, 2024, **12**, 8149–8154.

9 J.-H. Wang, S.-W. Yang, F.-B. Ma, Y.-K. Zhao, S.-N. Zhao, Z.-Y. Xiong, D. Cai, H.-D. Shen, K. Zhu, Q.-Y. Zhang, Y.-L. Cao, T.-S. Wang and H.-P. Zhang, *Tungsten*, 2024, **6**, 114–123.

10 Y. Luo, C. Liu, J. Liu, X. Liu, Y. Zhou, X. Ou, B. Weng, J. Jiang and B. Han, *Chem. Eng. J.*, 2024, **481**, 148494.

11 M.-H. Sun, M.-Y. Qi, C.-L. Tan, Z.-R. Tang and Y.-J. Xu, *Chin. Chem. Lett.*, 2023, **34**, 108022.

12 C. Lu, X. Cai, X. Liu, D. Tian, B. Li, J. Li and Z. Lou, *J. Mater. Chem. A*, 2024, **12**, 5909–5917.

13 J. Luo, M. Wang, L. Chen and J. Shi, *J. Energy Chem.*, 2022, **66**, 52–60.

14 C.-L. Tan, M.-Y. Qi, Z.-R. Tang and Y.-J. Xu, *Appl. Catal., B*, 2021, **298**, 120541.

15 Y.-L. Wu, M.-Y. Qi, C.-L. Tan, Z.-R. Tang and Y.-J. Xu, *Chin. J. Catal.*, 2022, **43**, 1851–1859.

16 H.-Q. Chen, J.-G. Hao, Y. Wei, W.-Y. Huang, J.-L. Zhang, T. Deng, K. Yang and K.-Q. Lu, *Catalysts*, 2023, **13**, 544.

17 H. Ma, Y. Liu, R. Xiong and J. Wei, *Chin. Chem. Lett.*, 2022, **33**, 1042–1046.

18 W. L. Jia, X. Wu, Y. Liu, J. Y. Zhao, Y. Zhang, P. F. Liu, Q. Cheng and H. G. Yang, *J. Mater. Chem. A*, 2022, **10**, 25586–25594.

19 H. Liu, F. Sun, X. Li, Q. Ma, G. Liu, H. Yu, W. Yu, X. Dong and Z. Su, *Composites, Part B*, 2023, **259**, 110746.

20 H. Zhang, H. Gu, X. Wang, S. Chang, Q. Li and W.-L. Dai, *Chem. Eng. J.*, 2023, **457**, 141185.

21 X. Zheng, Y. Song, Y. Liu, Y. Yang, D. Wu, Y. Yang, S. Feng, J. Li, W. Liu, Y. Shen and X. Tian, *Coord. Chem. Rev.*, 2023, **475**, 214898.

22 J. Hu, X. Li, J. Qu, X. Yang, Y. Cai, T. Yang, F. Yang and C. M. Li, *Chem. Eng. J.*, 2023, **453**, 139957.

23 W. L. Jia, W. J. Li, H. Y. Yuan, X. Wu, Y. Liu, S. Dai, Q. Cheng, P. F. Liu and H. G. Yang, *J. Energy Chem.*, 2022, **74**, 341–348.

24 A. Raja, N. Son, M. Swaminathan and M. Kang, *J. Colloid Interface Sci.*, 2021, **602**, 669–679.

25 S. Wang, B. Y. Guan, X. Wang and X. W. D. Lou, *J. Am. Chem. Soc.*, 2018, **140**, 15145–15148.

26 B. Ma, X. Li, D. Li and K. Lin, *Appl. Catal., B*, 2019, **256**, 117865.

27 S. Tang, Y. Xia, J. Fan, B. Cheng, J. Yu and W. Ho, *Chin. J. Catal.*, 2021, **42**, 743–752.

28 X. Zhang, M. Gao, L. Qiu, W. Yang and Y. Yu, *Chem. Eng. J.*, 2023, **465**, 142747.

29 K.-Q. Lu, Y.-H. Li, F. Zhang, M.-Y. Qi, X. Chen, Z.-R. Tang, Y. M. A. Yamada, M. Anpo, M. Conte and Y.-J. Xu, *Nat. Commun.*, 2020, **11**, 5181.

30 L. Wu, Q. Li, C. Yang, X. Ma, Z. Zhang and X. Cui, *J. Mater. Chem. A*, 2018, **6**, 20947–20955.

31 M.-Q. Yang, N. Zhang, M. Pagliaro and Y.-J. Xu, *Chem. Soc. Rev.*, 2014, **43**, 8240–8254.

32 Y. Dong, L. Kong, P. Jiang, G. Wang, N. Zhao, H. Zhang and B. Tang, *ACS Sustain. Chem. Eng.*, 2017, **5**, 6845–6853.

33 Q. Li, W. Feng, Y. Liu, D. Chen, Z. Wu and H. Wang, *J. Mater. Chem. A*, 2022, **10**, 15752–15765.

34 W. Yang, K. Sun, J. Wan, Y.-A. Ma, Y. Wang, L. Liu, B. Zhu and F. Fu, *Chem. Eng. J.*, 2023, **452**, 139425.

35 H. Su, C. Rao, L. Zhou, Y. Pang, H. Lou, D. Yang and X. Qiu, *Green Chem.*, 2022, **24**, 2027–2035.

36 Y.-H. Li, M.-Y. Qi, J.-Y. Li, Z.-R. Tang and Y.-J. Xu, *Appl. Catal., B*, 2019, **257**, 117934.

37 F. Yang, P. Hu, F. Yang, X.-J. Hua, B. Chen, L. Gao and K.-S. Wang, *Tungsten*, 2024, **6**, 77–113.

38 Y. Wu, Z. Wang, Y. Yan, Y. Wei, J. Wang, Y. Shen, K. Yang, B. Weng and K. Lu, *Molecules*, 2024, **29**, 465.

39 Y. Peng, X. Guo, S. Xu, Y. Guo, D. Zhang, M. Wang, G. Wei, X. Yang, Z. Li, Y. Zhang and F. Tian, *J. Energy Chem.*, 2022, **75**, 276–284.

40 Y. Peng, M. Geng, J. Yu, Y. Zhang, F. Tian, Y. Guo, D. Zhang, X. Yang, Z. Li, Z. Li and S. Zhang, *Appl. Catal., B*, 2021, **298**, 120570.

41 Y. Ma, G. Hai, J. Liu, J. Bao, Y. Li and G. Wang, *Chem. Eng. J.*, 2022, **441**, 136002.

42 X. Li, X. Wang, J. Zhu, Y. Li, J. Zhao and F. Li, *Chem. Eng. J.*, 2018, **353**, 15–24.

43 K.-Q. Lu, Y.-H. Li, Z.-R. Tang and Y.-J. Xu, *ACS Mater. Au*, 2021, **1**, 37–54.

44 K.-Q. Lu, J.-G. Hao, Y. Wei, B. Weng, S. Ge, K. Yang, S. Lu, M.-Q. Yang and Y. Liao, *Inorg. Chem.*, 2024, **63**, 795–802.

45 F. Xing, R. Zeng, C. Cheng, Q. Liu and C. Huang, *Appl. Catal., B*, 2022, **306**, 121087.

46 Q. Lin, Y.-H. Li, M.-Y. Qi, J.-Y. Li, Z.-R. Tang, M. Anpo, Y. M. A. Yamada and Y.-J. Xu, *Appl. Catal., B*, 2020, **271**, 118946.

47 P. Li, X. Yan, S. Gao and R. Cao, *Chem. Eng. J.*, 2021, **421**, 129870.

48 G. Sun, Z. Tai, F. Li, Q. Ye, T. Wang, Z. Fang, L. Jia, W. Liu and H. Wang, *Small*, 2023, **19**, 2207758.

49 N. Zhang, M.-Q. Yang, Z.-R. Tang and Y.-J. Xu, *ACS Nano*, 2014, **8**, 623–633.

50 H. Zhang, Y. Gao, S. Meng, Z. Wang, P. Wang, Z. Wang, C. Qiu, S. Chen, B. Weng and Y. Zheng, *Adv. Sci.*, 2024, 2400099.

51 B. Liu, J. Cai, J. Zhang, H. Tan, B. Cheng and J. Xu, *Chin. J. Catal.*, 2023, **51**, 204–215.

52 X. Wang, T. Shi, X. Wang, A. Song, G. Li, L. Wang, J. Huang, A. Meng and Z. Li, *J. Energy Chem.*, 2024, **92**, 151–161.

53 G. Z. Sheng Ling, S. H. Wan Kok, P. Zhang, T. J. Siang, C. Y. Haw, L.-L. Tan, B. Chen and W.-J. Ong, *J. Mater. Chem. A*, 2024, **12**, 1453–1464.

18992 | *J. Mater. Chem. A*, 2024, **12**, 18986–18992

This journal is © The Royal Society of Chemistry 2024